ADVANCED
FUNCTIONAL
MATERIALS

Supporting Information

for *Adv. Funct. Mater.,* DOI: 10.1002/adfm.202209273

Atomic Modulation and Structure Design of Fe−N_4 Modified Hollow Carbon Fibers with Encapsulated Ni Nanoparticles for Rechargeable Zn–Air Batteries

Yuhui Tian, Zhenzhen Wu, Meng Li, Qiang Sun, Hao Chen, Ding Yuan, Daijie Deng, Bernt Johannessen, Yun Wang, Yulin Zhong, Li Xu, Jun Lu, and Shanqing Zhang**

Supporting Information

Atomic Modulation and Structure Design of Fe−N_4 Modified Hollow Carbon Fibers with Encapsulated Ni Nanoparticles for Rechargeable Zn–Air Batteries

Yuhui Tian, Zhenzhen Wu, Meng Li, Qiang Sun, Hao Chen, Ding Yuan, Daijie Deng, Bernt Johannessen, Yun Wang, Yulin Zhong, Li Xu, Jun Lu*, Shanqing Zhang*

Experimental Section

Synthesis of nano-cuboid Ni precursor: The nano-cuboid Ni precursor was prepared according to a previously reported method with minor modifications.[1] Typically, 0.75 g of polyvinylpyrrolidone (PVP; K30, Sigma, MW ≈40000) and 0.35 g of nickel acetate tetrahydrate were dissolved in 50 mL of ethanol. The above solution was transferred to a 50 mL Teflon-lined stainless-steel autoclave and subjected to a hydrothermal reaction at 100 ℃ for 3 h. A light green precipitate was obtained after centrifuging five times at 5000 rpm, and subsequently dried overnight at 60 ℃ in a vacuum oven.

Synthesis of $\mathbf{Ni_{NP}}$@Ni-HCFs: First, 0.2 g of the prepared Ni precursors was dispersed in 2.5 mL of dimethylformamide (DMF) and mixed with 0.25 g of polyacrylonitrile (PAN, MW ≈150000) under overnight stirring at 60°C. Then, the Ni precursor/PAN/DMF solution was transferred into a syringe using a stainless needle tip. Subsequently, the Ni precursor-embedded PAN fibers were electrospun on an aluminum foil with a feeding rate of 0.8 mL h^{-1}. The distance between the stainless needle and collector was fixed at 12 cm, and the applied potential was 15 kV. The obtained Ni-precursor embedded PAN fibers were stabilized at 100 ℃ for 2 h. Then, the stabilized fibers were first annealed at 350 °C for 2 h and then carbonized at 900 ℃ for 2 h under Ar atmosphere at a ramping rate of 2 ℃ min^{-1}. The annealed sample, after cooling naturally, was designated as Ni_{NP}@Ni-HCFs. Carbon fibers were also synthesized by a similar method without the addition of the nano-cuboid Ni precursors.

Synthesis of Fe-N@Ni-HCFs: Typically, 0.198 g of $FeCl_2·4H_2O$ and 0.36 g of 1,10-phenanthroline (Phen) were dissolved in 100 mL ethanol to form the Fe-Phen complex at room temperature. Then, 0.4 g of Ni_{NP}@Ni-HCFs was immersed into the above solution and constantly stirred at 60 °C for 3 h. The residue was collected by filtration and dried overnight in a vacuum oven at 60 °C. The Fe-Phen impregnated Ni_{NP}@Ni-HCFs sample was calcined at 900 ℃ for 1 h with the ramping rate of 5 ℃ min^{-1} under Ar atmosphere. Subsequently, the obtained product was leached using 1 M HCl solution to remove the unstable species. Finally, the Fe-N@Ni-HCFs catalyst was obtained after direct annealing treatment at 800 °C for 15 min under vacuum to remove the anions or impurities adsorbed on the active sites during the etching process. This is because these adsorbed species might act as axial ligands, which might affect the electrocatalytic activity of the as-prepared catalyst. As a control sample, the Ni-HCFs catalyst was obtained after acid leaching of Ni_{NP}@Ni-HCFs and further thermal treatment at 800 °C under vacuum. The Fe-N@CFs catalyst was synthesized via a similar procedure, except that the Ni_{NP}@Ni-HCFs was replaced with carbon fibers as the host material.

Physical characterizations: Field-emission scanning electron microscopy (FESEM, JEOL JSM-7800F) and transmission electron microscopy (TEM, JEOL JEM-2010F) were utilized to evaluate the morphology of the prepared samples. The atomic-resolution spherical aberration-corrected TEM images were obtained by JEOL ARM-200F. The crystal structures were characterized by X-ray diffraction (Shimadzu, XRD-6100) using a high-intensity Cu Kα radiation source (λ=1.54 Å) and operating at a voltage of 40 kV and current of 30 mA. X-ray photoelectron spectroscopy (XPS) analysis was performed using a Thermo ESCALB 250XI X-ray photoelectron spectrometer. Specific surface areas and pore size distributions were obtained from nitrogen sorption isotherms at 77 K (Quantachrome Instrument Corporation). Fe and Ni K-edge X-ray absorption spectra were collected on the hard X-ray beamline at the Australian Synchrotron in Melbourne.

Electrochemical measurements: All electrochemical measurements were performed CHI 760E electrochemical workstation (CH Instrument) in a typical three-electrode system. A graphite rod and Ag/AgCl electrode (saturated KCl) were used as the counter electrode and reference electrode, respectively. The test of ORR and OER catalytic activity was conducted on the rotating ring disk electrode (RRDE) with a diameter of 4 mm. To prepare the working electrode, 5 mg of catalyst powder was dispersed into 1000 μL of 1:1 water/ethanol solution and 20 μL of Nafion solution (10 wt%), followed by ultrasonic treatment. Then, 5 μL of the catalyst ink was loaded onto the surface of glassy carbon in RRDE. All the potentials were calibrated to the reversible hydrogen electrode (RHE) according to the Nernst equation (Eqn. 1)

$$E_{\mathrm{RHE}} = E_{\mathrm{Ag/AgCl}} + 0.059\,pH + 0.197 \qquad (1)$$

Before ORR tests, oxygen was purged in the electrolyte for at least 30 min to ensure oxygen saturation in the electrolyte. Cyclic voltammetry (CV) was performed at the scan rate of 50 mV s^{-1}. Linear sweep voltammetry (LSV) curves were recorded with a scan rate of 5 mV s^{-1}, and the capacitive current was eliminated. For RRDE tests, the ring electrode potential was set to 1.25 V (vs. RHE) to oxidize HO_2^- intermediate from the disk electrode. The electron transfer number and the percentage of HO_2^- were calculated according to Eqns. 2–3:

$$n = 4|I_d|/(|I_d| + I_r/N) \qquad (2)$$

$$\mathrm{HO_2^-} = 200 \times I_r / (I_r + N|I_d|) \qquad (3)$$

Where I_d is the disk current, I_r represents the ring current, and N is the current collection efficiency of the Pt ring with a value of 0.37.

The kinetic current density (j_k) was calculated to the equation:

$$1/j_m = 1/j_L + 1/j_k \qquad (4)$$

where j_m indicates the measured total current density and j_L is the diffusion-limiting current density. The value of j_L is usually determined by the highest steady current measured in the entire potential range.

The electron transfer number per oxygen molecule was also calculated from the Koutecky–Levich (K–L) equations (Eqns. 5–6):

$$\frac{1}{j} = \frac{1}{j_k} + \frac{1}{B}\omega^{-1/2} \qquad (5)$$

$$B = 0.2nF(D_{(O_2)})^{2/3} v^{(-1/6)} C_{(O_2)} \qquad (6)$$

ω is the angular velocity of the disk (rpm).

n is the electron transfer number for ORR.

F is Faraday constant (96485 C mol^{-1}).

$D_{(O_2)}$ is the diffusion coefficient of O_2 in 0.1 M KOH (1.9×10^{-5} cm^2 s^{-1}).

v is the kinematic viscosity (0.01 cm^2 s^{-1}).

$C_{(O_2)}$ is the bulk concentration of O_2 in the solution (1.2×10^{-6} mol cm^{-3}).

The OER tests were conducted in 0.1 M KOH. LSV curves were recorded with a scan rate of 5 mV s^{-1}. Electrochemical impedance spectroscopy (EIS) measurements were carried out by applying an AC voltage with 5 mV amplitude in a frequency range from 100 kHz to 0.1 Hz at the potential of 1.60 V (vs. RHE) in 0.1 M KOH. The double-layer capacitance (C_{dl}) of catalysts was investigated on the basis of CV curves recorded at different sweep rates (2, 4, 6, 8, 10, and 12 mV s^{-1}) in the potential range of 1.20−1.26 V (vs. RHE). The chronoamperometry tests were performed under 0.4 V (vs. RHE) for ORR and 1.60 V (vs. RHE) for OER.

Tafel slopes were calculated from the Tafel equation:

$$\eta = \mathrm{b} \log(j/j_0) \qquad (7)$$

where η is the potential, b is the Tafel slope, j is the current density, and; j_0 is the exchange current density.

Computational details: The density functional theory (DFT) calculations were performed in the Vienna ab initio simulation packages (VASP),[2] using the generalized gradient approximation (GGA) with Perdew–Burke–Ernzerhof (PBE) parameterization.[3] The in-plane lattice parameters of graphene (2.46 Å), Co(111) (2.51 Å), Ni(111) (2.49 Å), and Cu(111) (2.55 Å) are very close.[4] Thus, the lattice mismatch is less than 4% when coupled to construct the heterostructure. In order to incorporate the atomic Fe−N_4 site into the periodic graphene layer, six C atoms on the 4×4 single-layer graphene unit cell were replaced by four N atoms and a single Fe atom. The Fe atom was located at the center of four N atoms. A 4×4 supercell slab containing four layers was constructed for Co/Ni/Cu(111), where the last two layers of metal atoms were fixed. The single-layer graphene containing the Fe−N_4 site was placed on the top of Co/Ni/Cu(111) slab to construct the Fe−N_4−C||Co/Ni/Cu models. A vacuum space of 20 Å was set to eliminate possible interaction between the periodic images. The Brillouin zone integrations were performed with a Gamma-center 3×3×1 k-point mesh for geometry optimization. The energy cut-off of the plane wave basis was set as 400 eV. The semi-empirical dispersion corrected DFT-D3 scheme proposed by Grimme was used to describe the van der Waals interactions.[5] Spin-polarization was applied for all the calculations. During the geometry optimization, the energy change criterion was set to 10^{-5} eV, and the maximum force was 0.03 eV $Å^{-1}$.

The four-electron ORR process based on the associative mechanism can be described below (Eqns. 8–11):

$$O_2(g) + * + H_2O\ (l) + e^- \leftrightarrow OOH* + OH^- \qquad (8)$$

$$OOH* + e^- \leftrightarrow O* + OH^- \qquad (9)$$

$$O* + H_2O\ (l) + e^- \leftrightarrow OH* + OH^- \qquad (10)$$

$$OH* + e^- \leftrightarrow * + OH^- \qquad (11)$$

where * represents an active site on the surface.

The free energies of ORR/OER intermediates are defined as $\Delta G = \Delta E + \Delta ZPE - T\Delta S$, where ΔE, ΔZPE, T, and ΔS represent the reaction energy, zero-point energy change, temperature (298.15 K), and the entropy change, respectively. The effect of the electrode potential on the free energy can be applied by shifting ΔG by $-eU$, where e and U are the elementary charge and applied electrode potential, respectively.

Liquid Zn–air battery assembly: The Zn–air battery tests were performed with a homemade Zn–air cell. The Fe-N@Ni-HCFs catalyst layer was placed on the gas diffusion layer (GDL) with a mass loading of ~1 mg cm^{-2} and then cold-pressed at a pressure of 4 Mpa to fabricate the cathode. A stainless steel mesh was fixed on the GDL as the current collector, while polished Zn foil was used as the anode. The mixed solution containing 6 M KOH and 0.2 M zinc acetate was used as the electrolyte. The discharge and charge polarization curves were recorded by linear sweep voltammetry at a sweep rate of 10 mV s^{-1}. Galvanostatic tests were conducted at a discharge current density of 10 mA cm^{-2}. The specific capacity and energy density were calculated from the galvanostatic discharge results and normalized to the mass of consumed Zn. The cycling test was conducted at a current density of 10 mA cm^{-2} (10 min for discharge and 10 min for charge in each cycle).

Flexible Zn–air battery Assembly: A polished Zn plate was tailored to a dimension of 1.5 × 2.5 cm with an extra portion for connection as the anode. The Fe-N@Ni-HCFs integrated GDL (1 × 2 cm) was used as the cathode. Nickel foam was fixed to the cathode as the current collector. The gel polymer electrolyte was prepared as follows: polyvinyl alcohol (PVA, MW 19500, Aladdin) powder (1.0 g) was dissolved in 10.0 mL of deionized water at 95 °C under magnetic stirring until a clear solution was obtained. Then 1.0 mL of 18.0 M KOH containing 0.1 M zinc acetate was added and stirred at 95 °C for 1.0 h. The solution was frozen at −3 °C for 12 h and then thawed at room temperature. Subsequently, the obtained gel electrolyte was tailored to a size of 1.5 × 2.5 cm and placed between the anode and cathode. Finally, the battery was constructed after sealing it with white breathable tape.

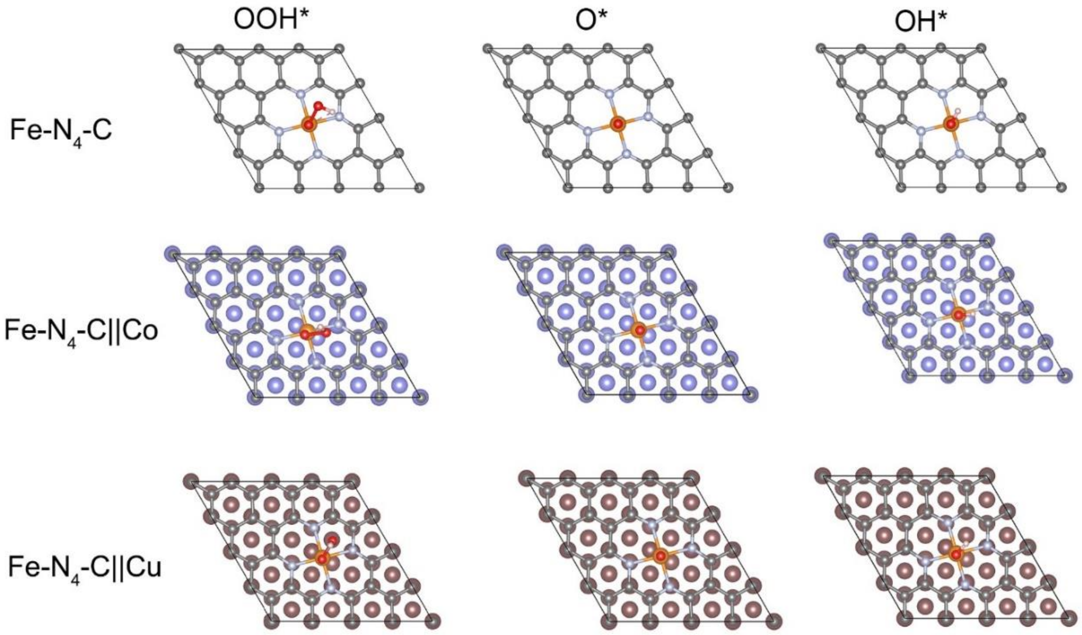

Figure S1. The optimized structure models of Fe−N$_4$−C, Fe−N$_4$−C||Co, and Fe−N$_4$−C||Cu with oxygenated intermediates (OOH*, O*, and OH*). Colour code: H, C, N, O, Fe, Co, and Cu atoms are represented in pink, grey, silver, red, orange, purple, and brown, respectively.

Table S1. The computed adsorption free energies for OH*, O*, and OOH* on different catalyst models.

Catalyst model	ΔG_{OH^*} (eV)	ΔG_{O^*} (eV)	ΔG_{OOH^*} (eV)
Fe−N_4−C	0.55	1.35	3.39
Fe−N_4−C‖Co	0.96	2.00	3.93
Fe−N_4−C‖Ni	0.95	1.92	3.81
Fe−N_4−C‖Cu	0.97	1.87	3.86

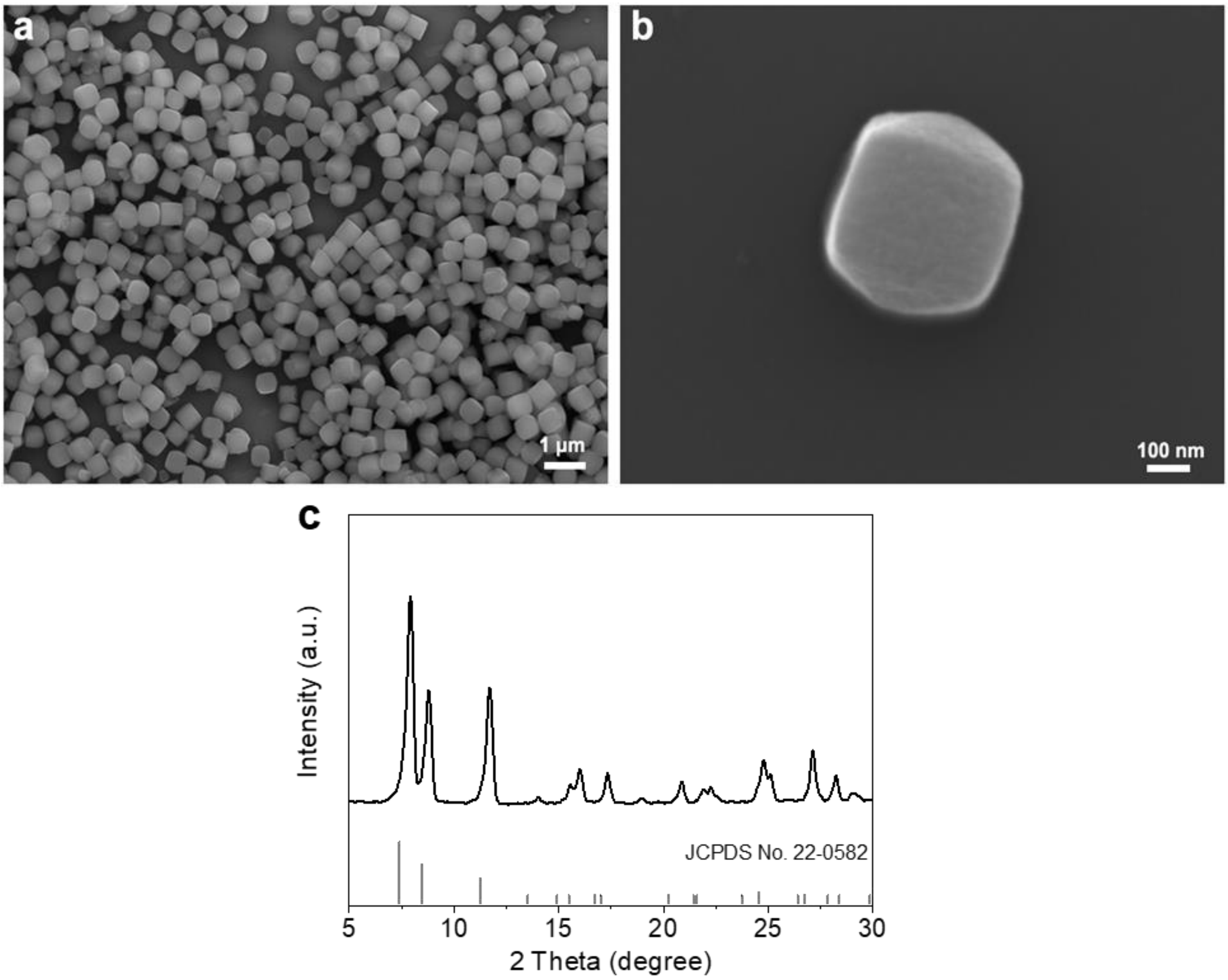

Figure S2. a-b) SEM images of nano-cuboid Ni precursors. c) XRD pattern of nano-cuboid Ni precursors showing a similar crystallographic structure to tetragonal cobalt acetate hydroxide (JCPDS No. 22-0582).

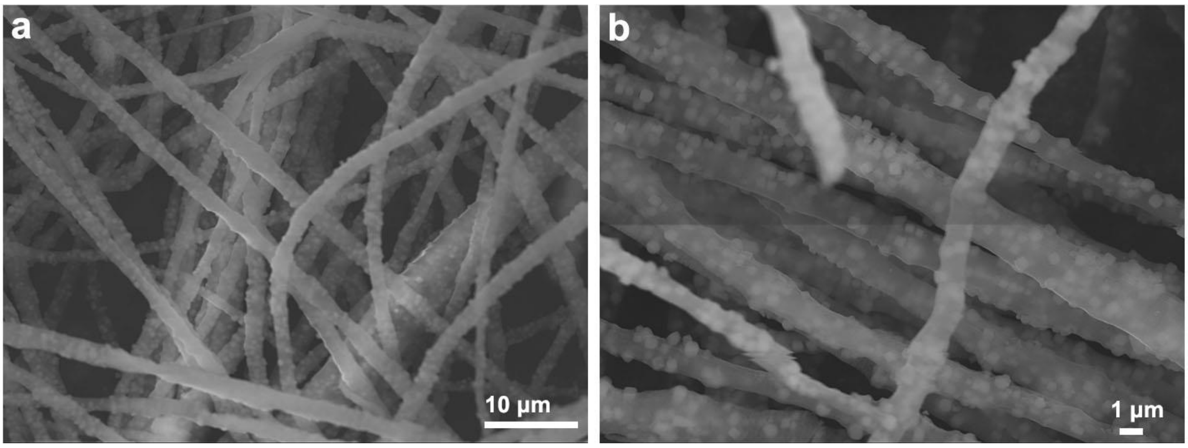

Figure S3. a-b) SEM images of Ni-PAN fibers (Ni@PFs).

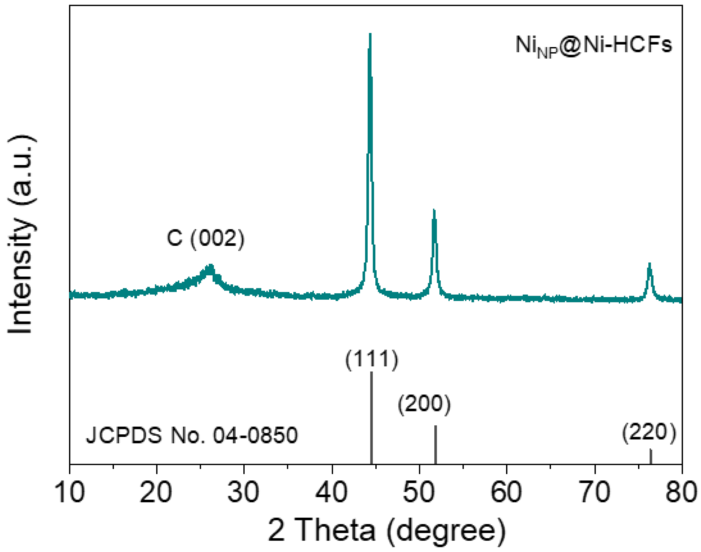

Figure S4. XRD pattern of Ni$_{NP}$@Ni-HCFs.

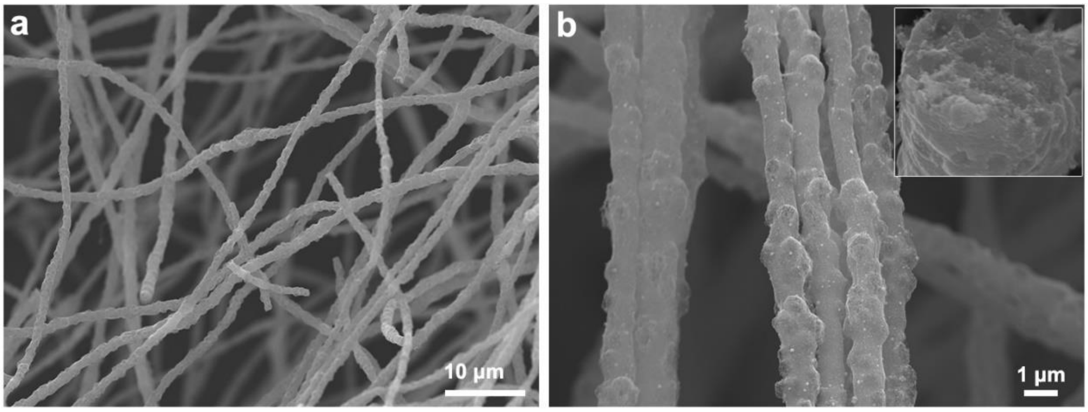

Figure S5. a-b) SEM images of Ni_{NP}@Ni-HCFs (inset: cross profile of Ni_{NP}@Ni-HCFs).

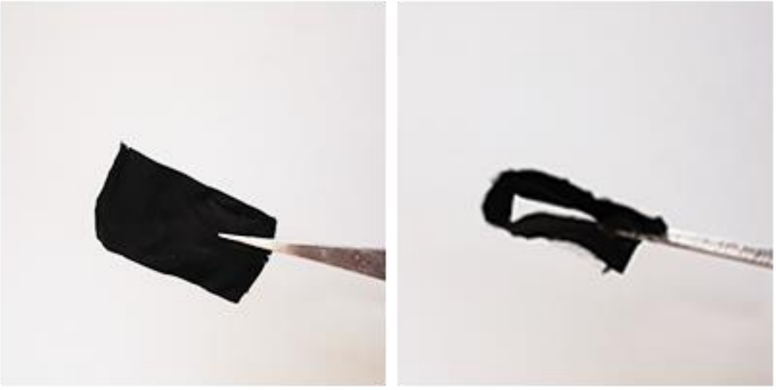

Figure S6. Digital photos of Fe-N@Ni-HCFs under flat (left) and bending state (right).

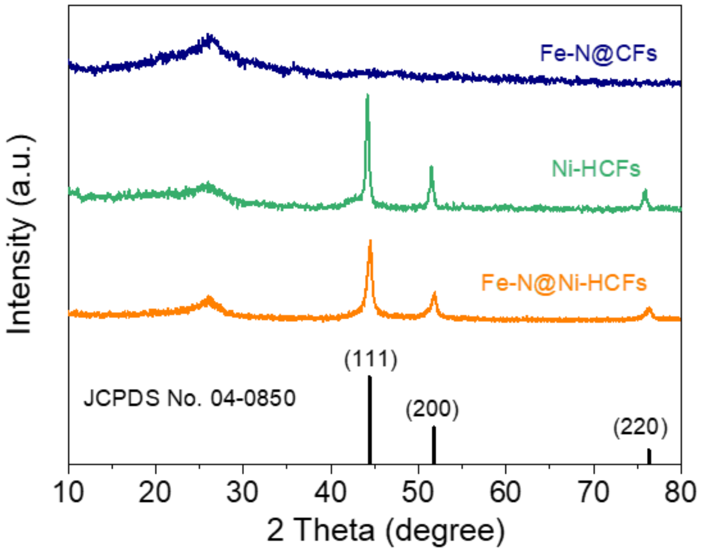

Figure S7. XRD patterns of Ni-HCFs, Fe-N@CFs, and Fe-N@Ni-HCFs.

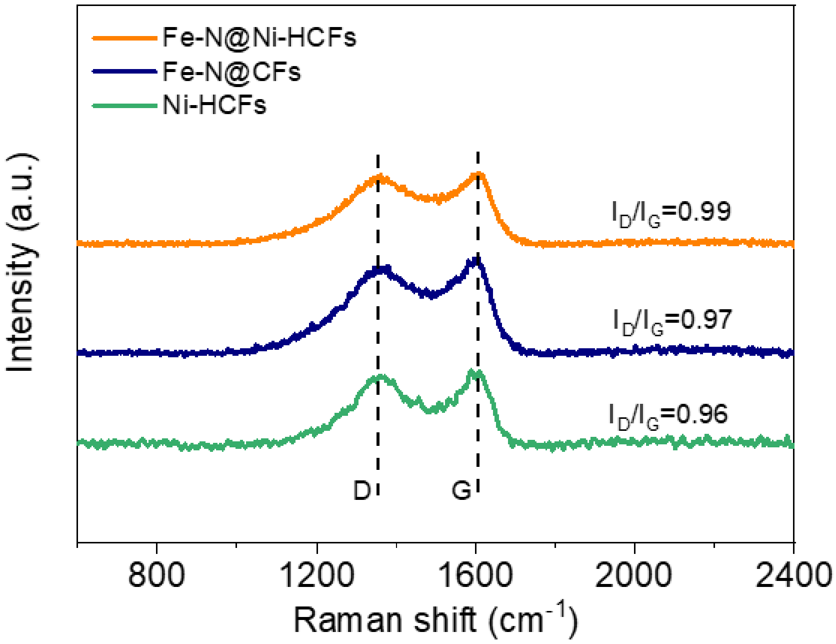

Figure S8. Raman spectra of Fe-N@Ni-HCFs, Fe-N@CFs, and Ni-HCFs.

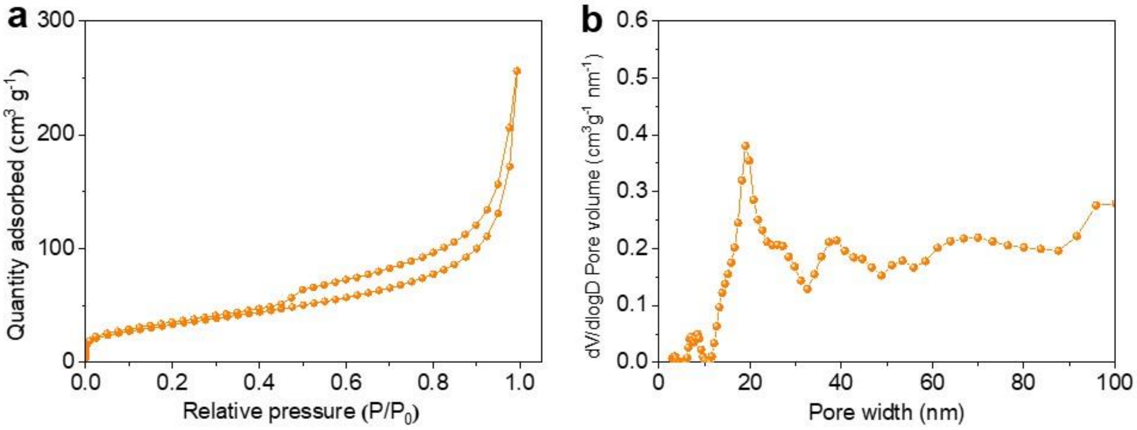

Figure S9. (a) N_2 adsorption-desorption isotherm and (b) corresponding pore size distribution of Fe-N@Ni-HCFs.

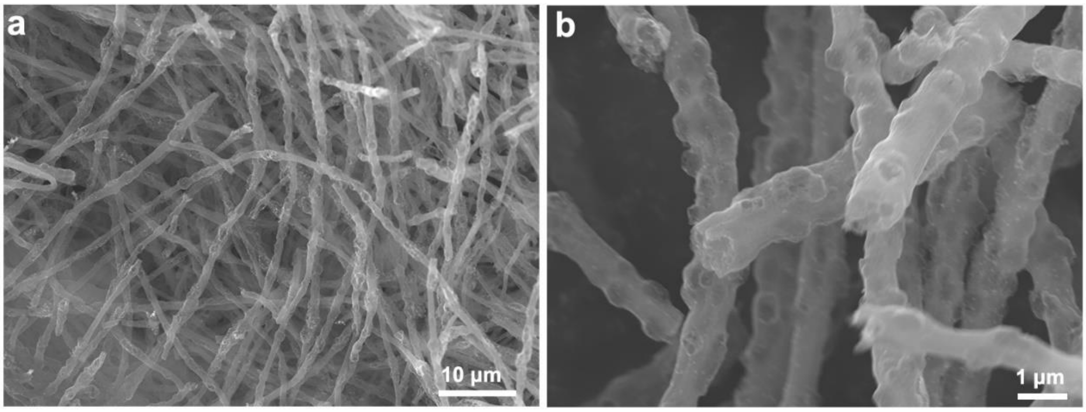

Figure S10. a-b) SEM images of Ni-HCFs.

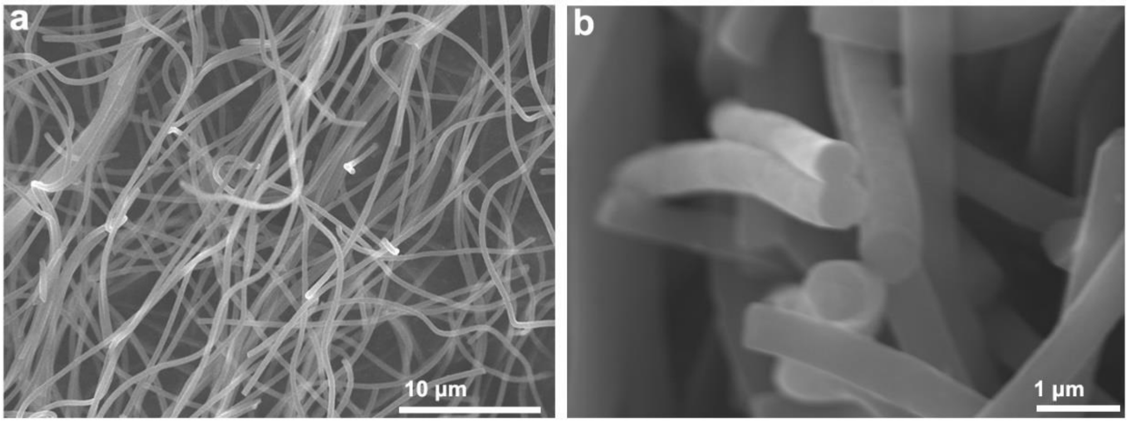

Figure S11. a-b) SEM images of Fe-N@CFs.

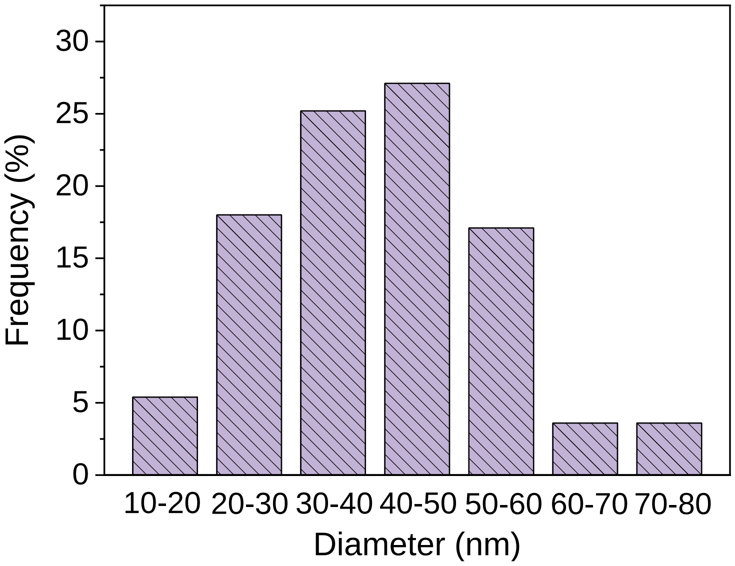

Figure S12. Size distribution of Ni nanoparticles in Fe-N@Ni-HCFs measured by TEM image.

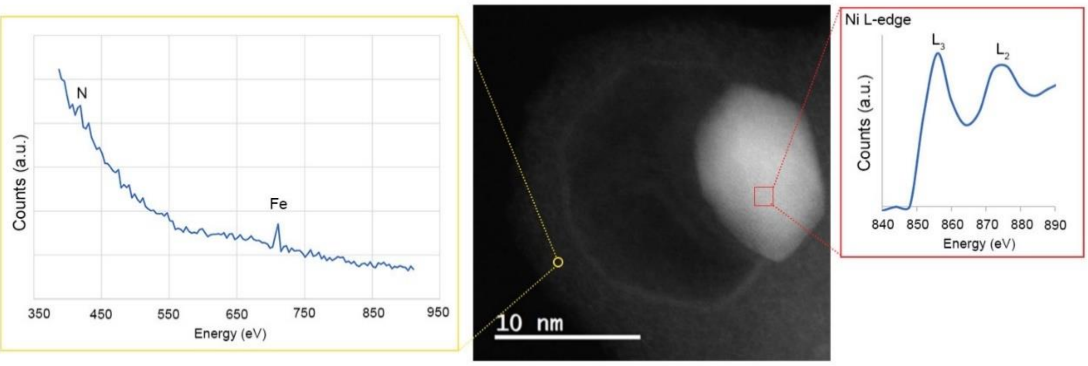

Figure S13. The STEM image of Fe-N@Ni-HCFs and corresponding EELS spectra of selected regions.

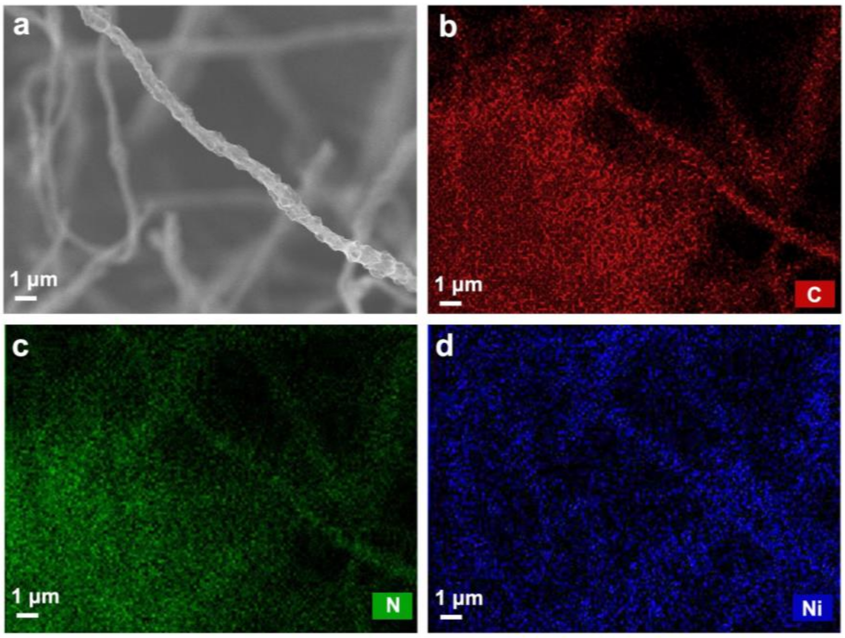

Figure S14. a) SEM image, b-d) SEM-EDS elemental mappings of Ni-HCFs, showing the presence of C, N, and Ni.

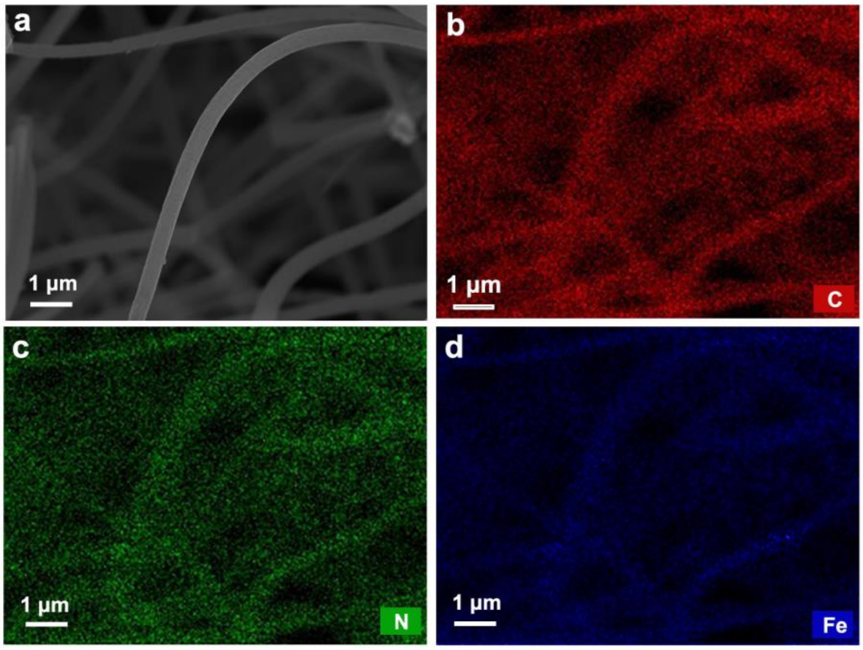

Figure S15. a) SEM image, b-d) SEM-EDS elemental mappings of Fe-N@CFs, showing the presence of C, N, and Fe.

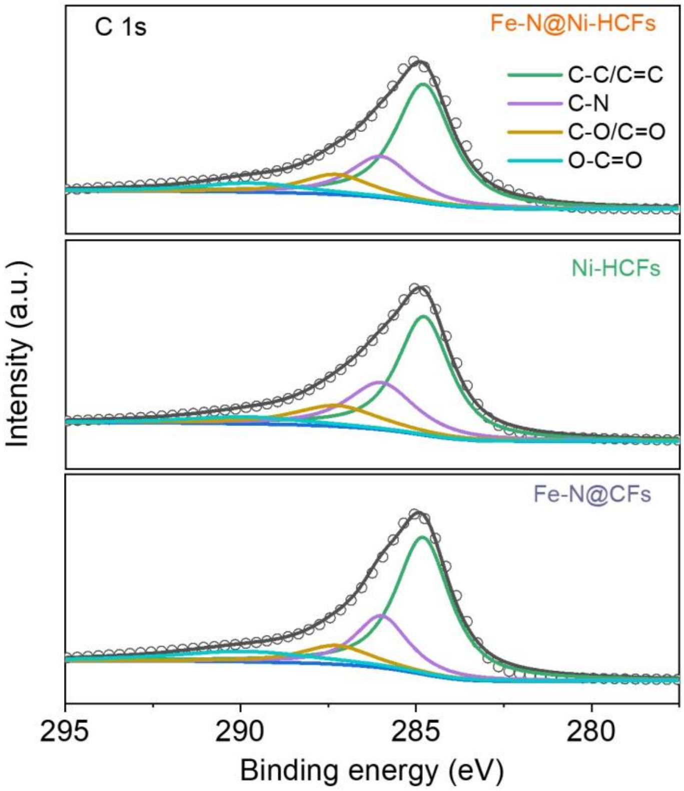

Figure S16. C 1s XPS spectra of Fe-N@Ni-HCFs, Ni-HCFs, and Fe-N@CFs.

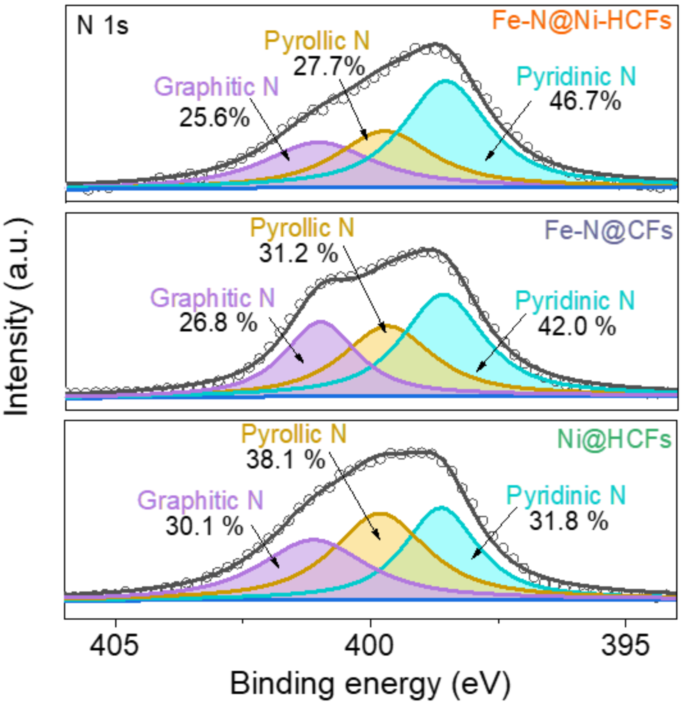

Figure S17. XPS N 1s spectra of Fe-N@Ni-HCFs, Fe-N@CFs, and Ni-HCFs

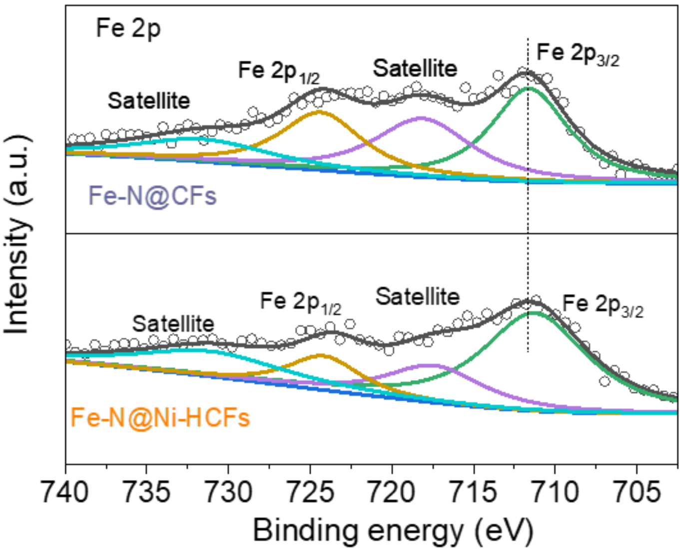

Figure S18. The comparison of XPS Fe 2p spectra of Fe-N@Ni-HCFs and Fe-N@CFs.

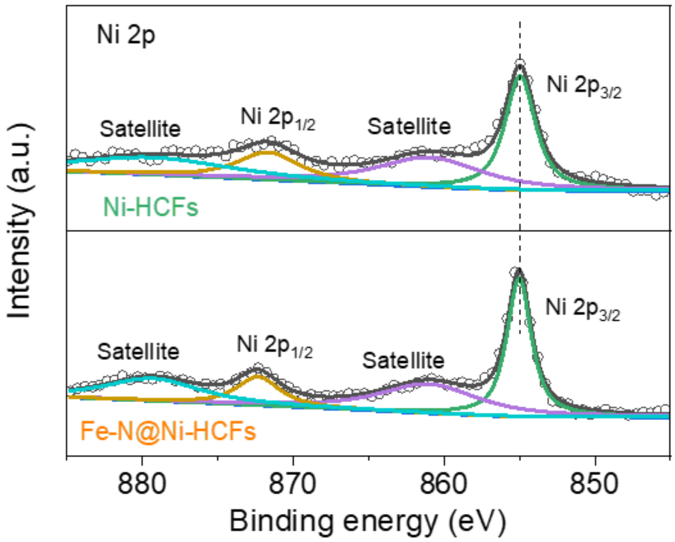

.

Figure S19. The comparison of XPS Ni 2p spectra of Fe-N@Ni-HCFs and Ni-HCFs.

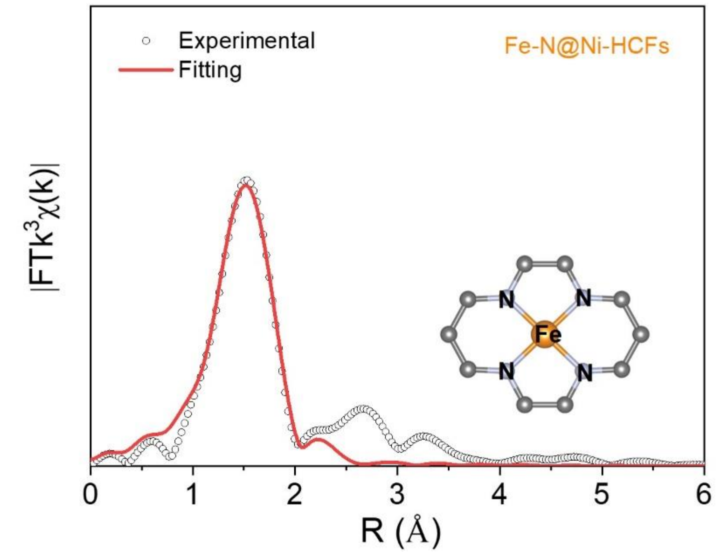

Figure S20. Fe K-edge FT-EXAFS fitting curve of Fe-N@Ni-HCFs based on the Fe−N_4−C configuration (inset).

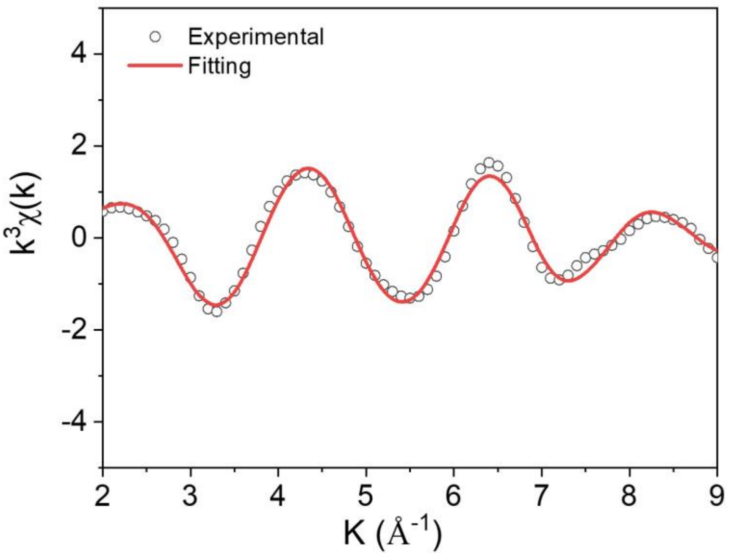

Figure S21. Corresponding EXAFS fitting curve of Fe-N@Ni-HCFs at *K* space.

Table S2. Fitting parameters of Fe K-edge FT-EXAFS.

Sample	**Scattering pair**	**CN**	**R(Å)**	**σ(Å^2)**	**ΔE_0 (eV)**	**R factor**
Fe-N@Ni-HCFs	Fe−N	3.82	2.00	0.01220	0.57	0.014

CN is the coordination number; R is the interatomic distance; σ is the Debye-Waller factor; ΔE_0 is the inner potential correction; R factor indicates the goodness of the fitting.

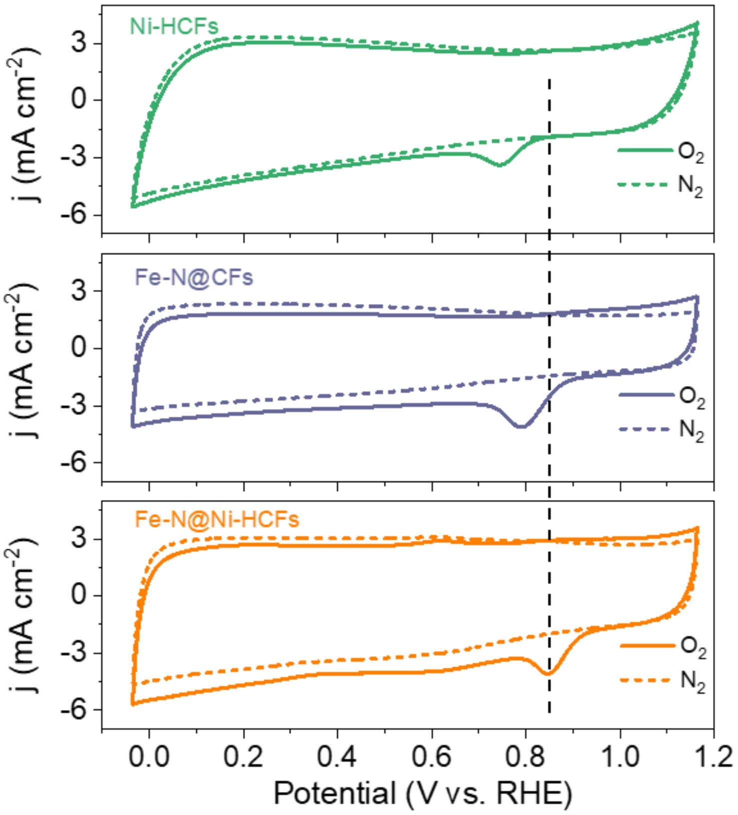

Figure S22. CV curves of Fe-N@Ni-HCFs, Ni-HCFs, and Fe-N@CFs in O_2- (solid line) and N_2-saturated (dash line) 0.1 M KOH at a scan rate of 50 mV s^{-1}.

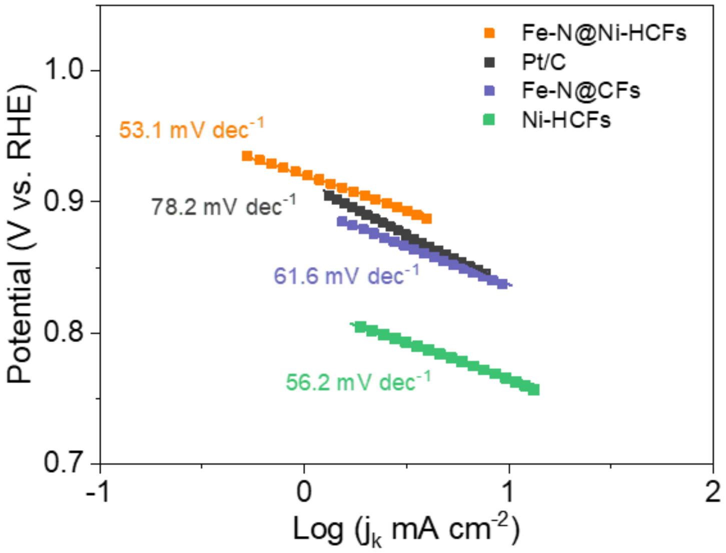

Figure S23. Tafel plots of Fe-N@Ni-HCFs, Ni-HCFs, Fe-N@CFs, and Pt/C for ORR.

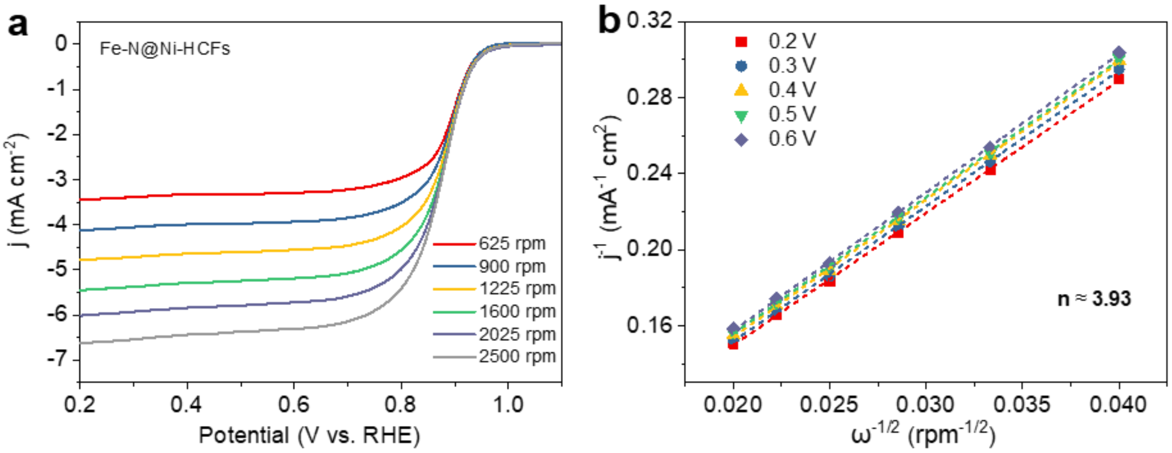

Figure S24. a) ORR LSV curves in O_2-saturated 0.1 M KOH with different rotation rates (625–2500 rpm) and b) the corresponding Koutecky-Levich plots (right) obtained at 0.2, 0.3, 0.4, 0.5, and 0.6 V for Fe-N@Ni-HCFs.

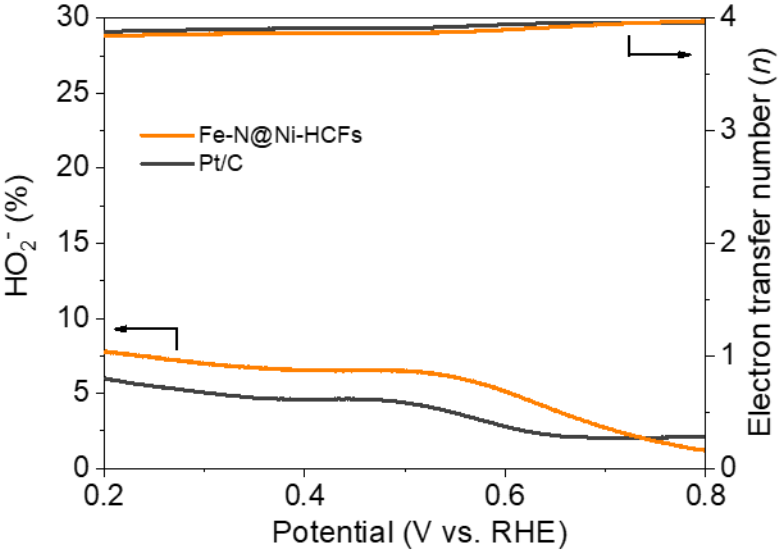

Figure S25. Calculated HO_2^- yield (%) and electron transfer number (n) of Fe-N@Ni-HCFs and Pt/C in O_2-saturated 0.1 M KOH.

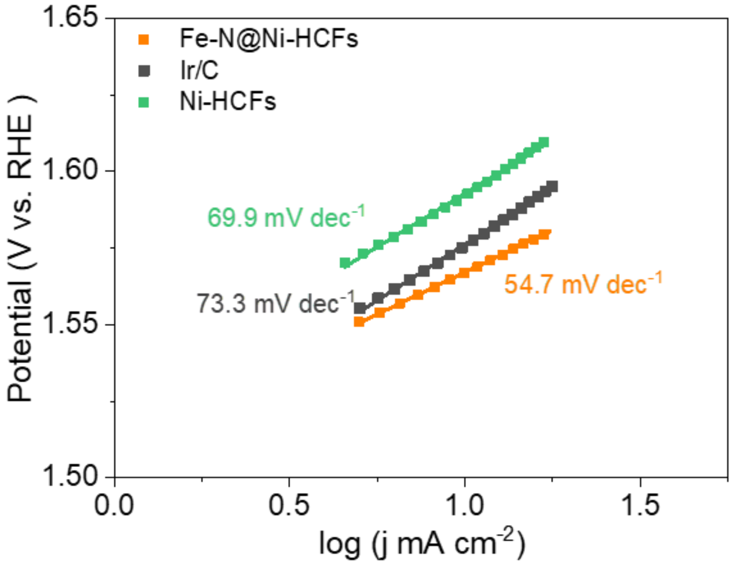

Figure S26. Tafel plots of Fe-N@Ni-HCFs, Ni-HCFs, and Ir/C for OER.

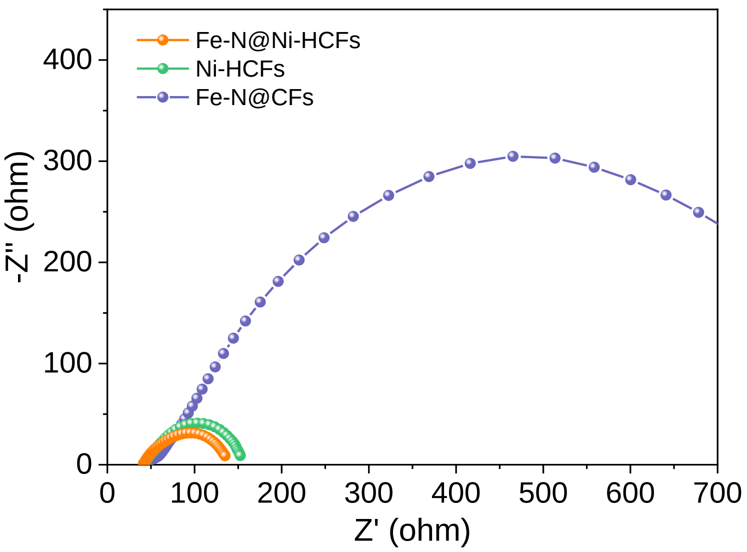

Figure S27. EIS Nyquist plots of Fe-N@Ni-HCFs, Ni-HCFs, and Fe-N@CFs for OER at the anodic potential value of 1.60 V (vs. RHE) in 0.1 M KOH.

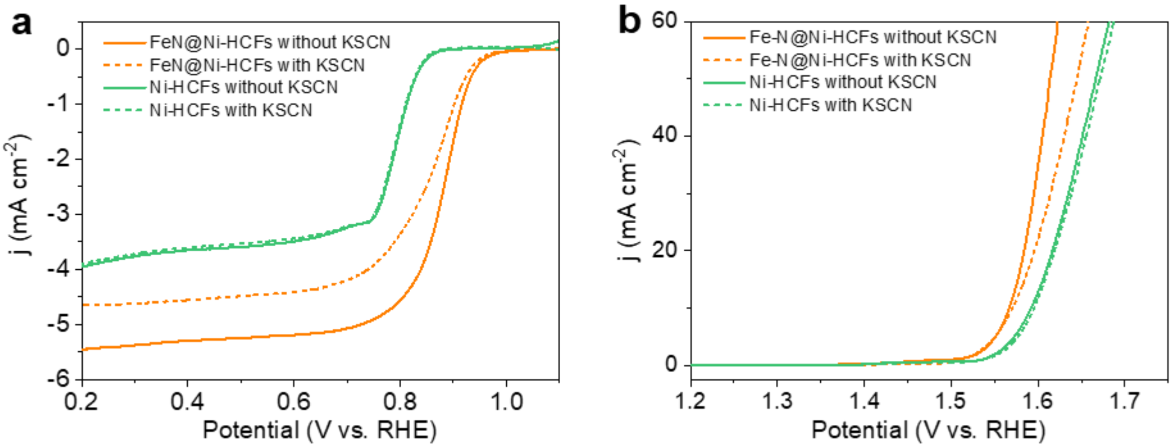

Figure S28. a) ORR and b) OER LSV curves of Fe-N@Ni-HCFs and Ni-HCFs under a rotation rate of 1600 rpm in the electrolyte with and without 10 mM KSCN.

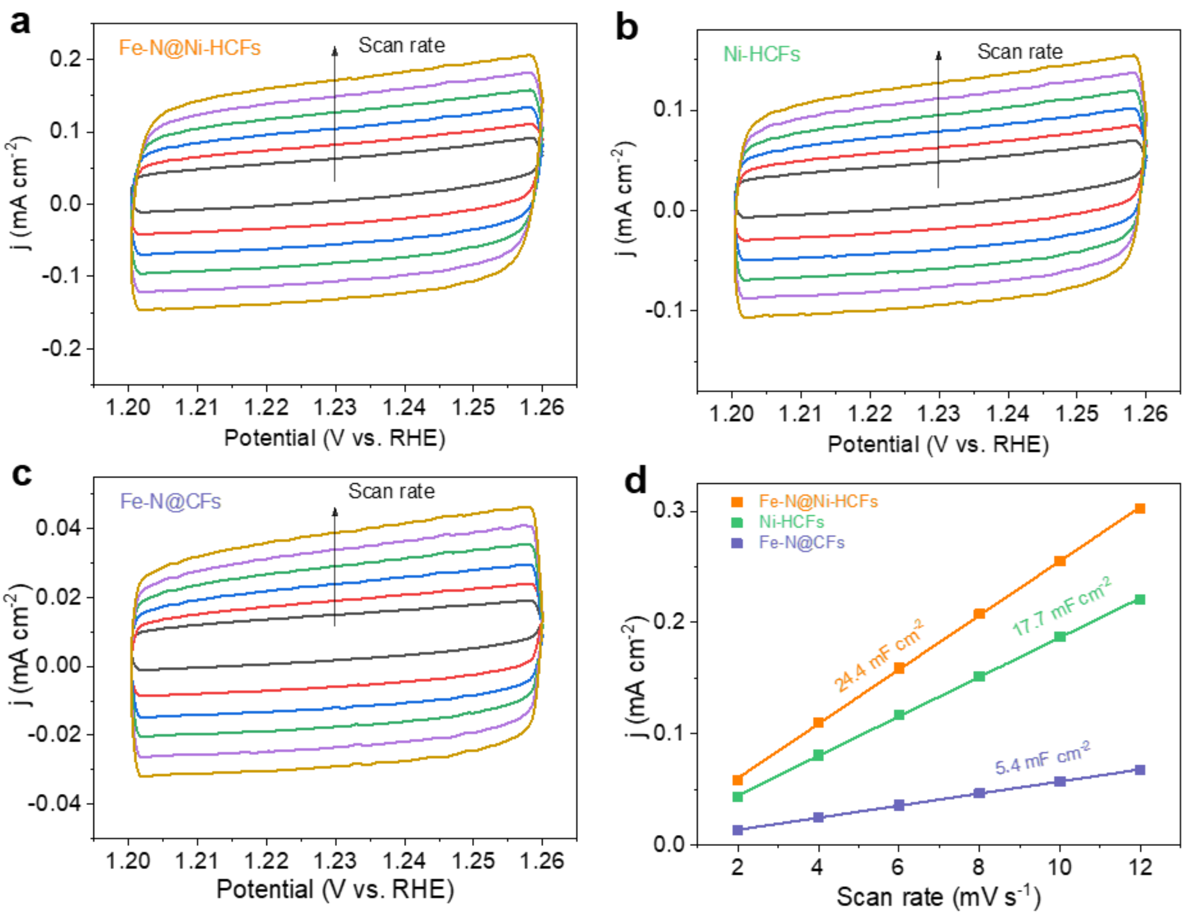

Figure S29. The CV curves of a) Fe-N@Ni-HCFs, b) Ni-HCFs, and c) Fe-N@CFs at the potential region of 1.20–1.26 V (vs. RHE) in 0.1 M KOH. d) The corresponding electrochemical double-layer capacitances.

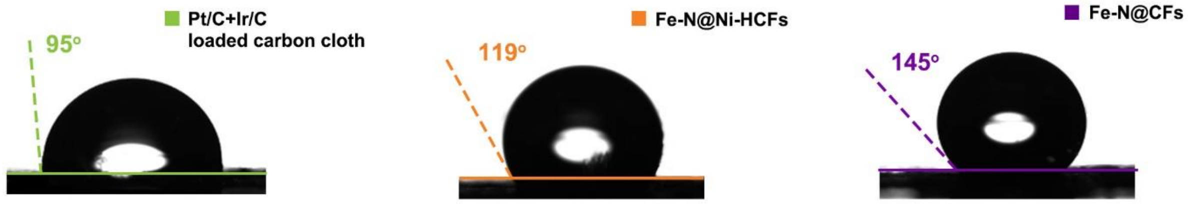

Figure S30. Contact angle measurements of Pt/C+Ir/C, Fe-N@CFs, and Fe-N@Ni-HCFs electrodes.

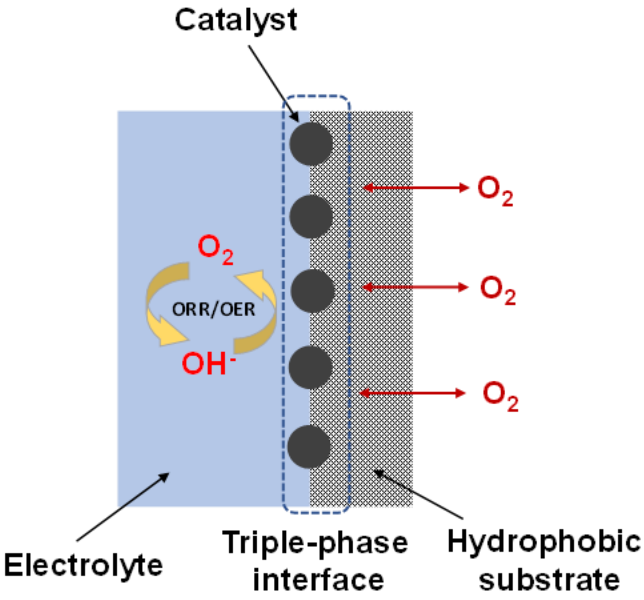

Figure S31. Schematic illustration of the triple-phase (i.e., liquid electrolyte, O_2 gas, and solid catalyst) electrocatalytic system. Pt/C+Ir/C loaded carbon cloth, Fe-N@CFs, and Fe-N@Ni-HCFs catalysts were pressed on the hydrophobic gas diffusion layer (GDL) as the electrode for electrochemical tests.

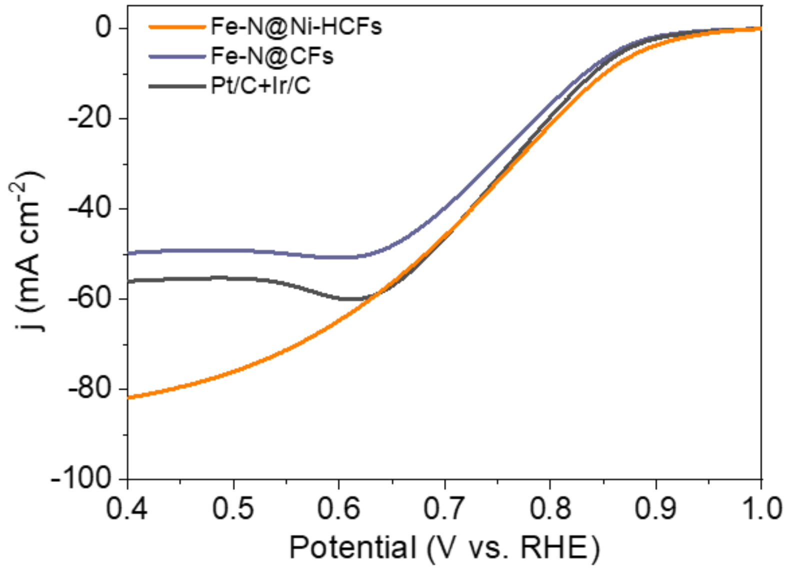

Figure S32. ORR LSV curves of Fe-N@CFs, Fe-N@Ni-HCFs, and Pt/C+Ir/C electrodes in the three-phase electrocatalytic system without O_2 pumping.

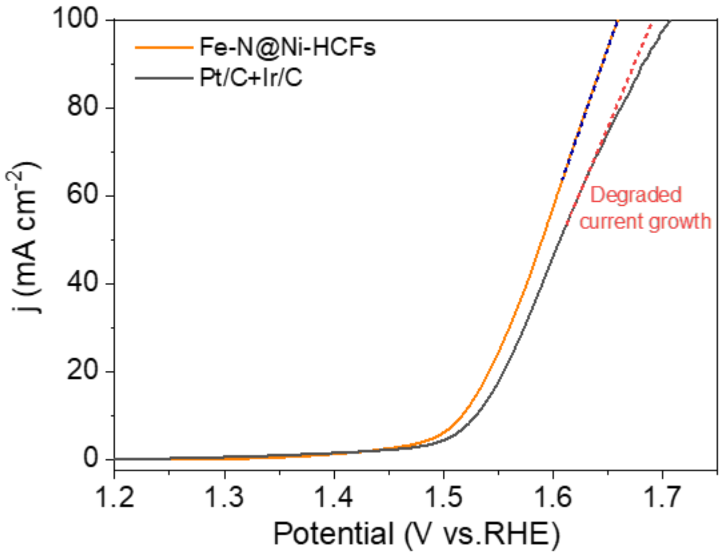

Figure S33. OER LSV curves of Fe-N@Ni-HCFs and Pt/C+Ir/C electrodes in the three-phase electrocatalytic system.

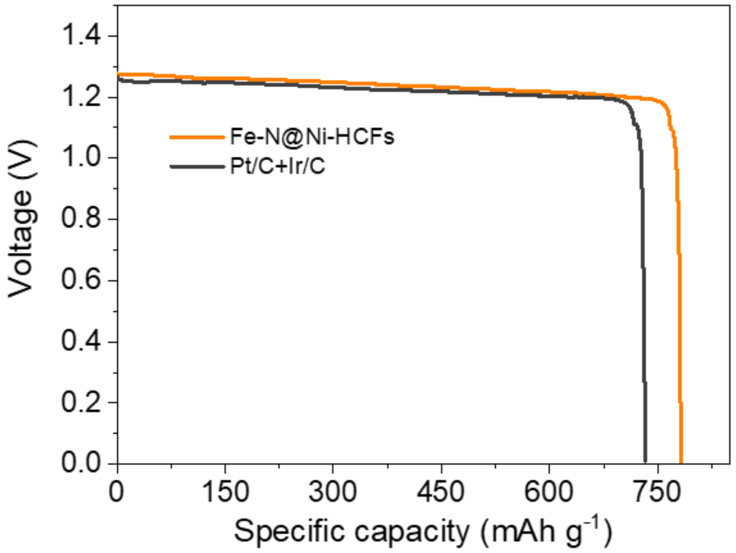

Figure S34. Galvanostatic discharge curves of the assembled liquid ZABs at the current density of 10 mA cm^{-2}.

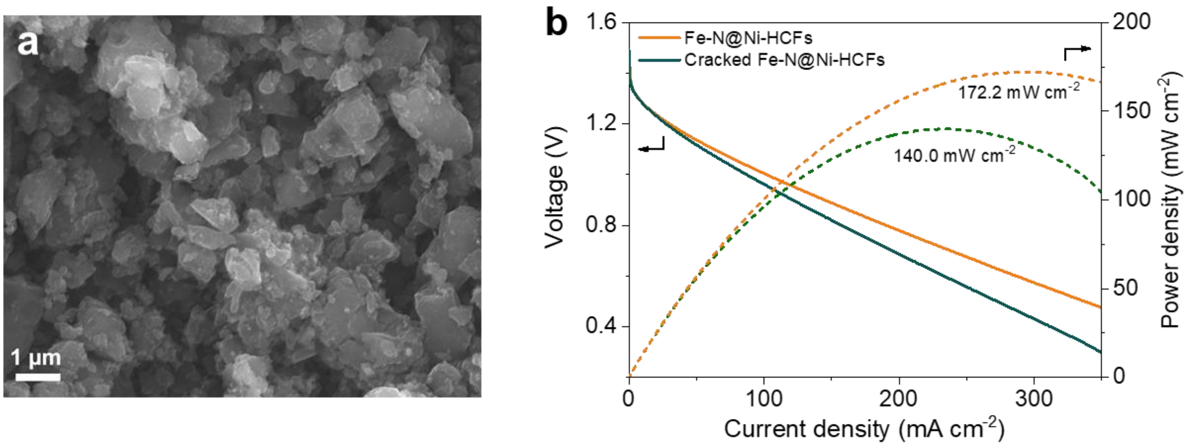

Figure S35. a) SEM image of the cracked Fe-N@Ni-HCFs. b) Discharge polarization curves and corresponding power density plots of ZABs with intact and cracked Fe-N@Ni-HCFs.

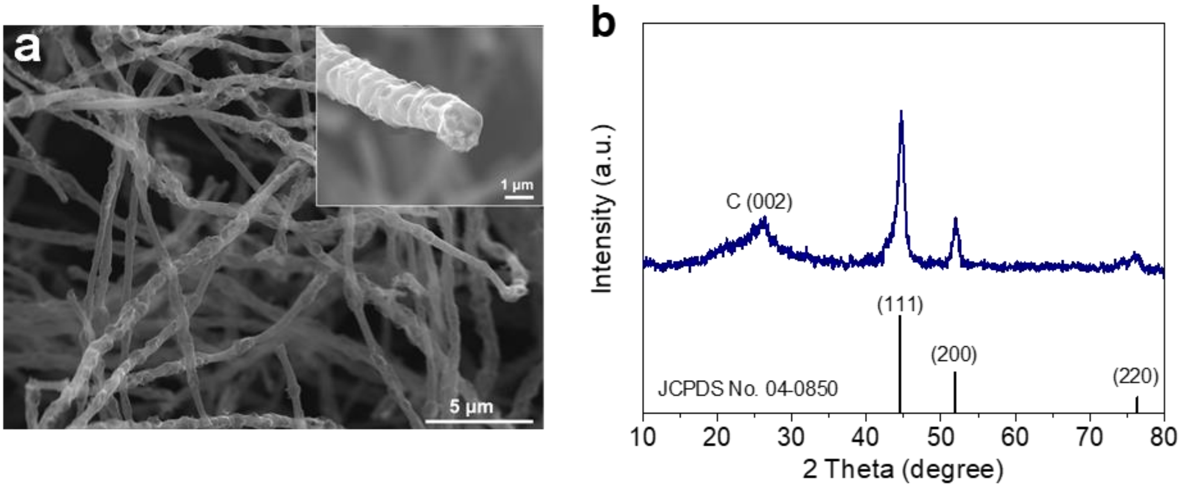

Figure S36. a) SEM image of the Fe-N@Ni-HCFs after cycling (inset: the image showing the well-maintained lotus root-like channels at the cross-section). b) XRD pattern of Fe-N@Ni-HCFs after cycling.

Table S3. The comparison of the bifunctional ORR/OER performance of Fe-N@Ni-HCFS with recently reported bifunctional electrocatalysts in KOH electrolytes.

Catalysts	**$E_{1/2}$ (V)**	**$E_{j=10}$ (V)**	**ΔE (V)**	**Reference**
Fe-N@Ni-HCFs	0.88, 0.1 M KOH	1.567, 0.1 M KOH	0.687	**This work**
FC-Ni_3N/NCNT	0.70, 0.1 M KOH	1.49, 0.1 M KOH	0.79	[6]
NiFe/N-CNT	0.75, 0.1 M KOH	1.52, 0.1 M KOH	0.77	[7]
Ni_3FeN	0.78, 0.1 M KOH	1.585, 0.1 M KOH	0.805	[8]
Ni-N_4/GHS/Fe-N_4	0.83, 0.1 M KOH	1.62, 0.1 M KOH	0.79	[9]
Fe/Ni-N_x/OC	0.938 V, 0.1 M KOH	1.668, 1 M KOH	0.73	[10]
Fe-NiNC-50	0.85, 0.1 M KOH	1.57, 1 M KOH	0.73	[11]
$Cu_{6.81}$-CoFS	0.80, 0.1 M KOH	1.54, 0.1 M KOH	0.74	[12]
CoNi-SAs/NC	0.76, 0.1 M KOH	1.57, 0.1 M KOH	0.81	[13]
Fe_1Co_1-CFS	0.87, 0.1 M KOH	1.73, 0.1 M KOH	0.86	[14]
FeCo/Co_2P@NPCF	0.79, 0.1 M KOH	1.56, 0.1 M KOH	0.77	[15]
FeNiCo@NC-P	0.84, 0.1 M KOH	1.54, 0.1 M KOH	0.70	[16]
Co/CoFe@NC	0.84, 0.1 M KOH	1.54, 1 M KOH	0.70	[17]
Fe_2Ni_2N/Co@NCNT	0.80, 0.1 M KOH	1.51, 1 M KOH	0.71	[18]
FeMn-DSAC	0.922, 0.1 M KOH	1.635, 0.1 M KOH	0.713	[19]

Table S4. The comparison of Zn–air battery performances of Fe-N@Ni-HCFS with recently reported bifunctional electrocatalysts in alkaline media.

Catalysts	**Open-circuit voltage (V)**	**Specific capacity (mAh g^{-1}) | current density (mA cm^{-2})**	**Peak power density (mW cm^{-2})**	**Reference**
Fe-N@Ni-HCFs	1.51	782.8 | 10	172.2	This work
FC-Ni$_3$N/NCNT	-	-	139.5	[6]
Ni-N$_4$/GHSs/Fe-N$_4$	1.45	777.6 14 | 5	-	[9]
Fe-NiNC-50	1.41	752.14 | 5	220	[11]
CoNi-SAs/NC	1.45	750.9 | 20	101.4	[13]
FeNiCo@NC-P	1.36	807 | 10	112	[16]
CoFe@Fe$_3$N-CNT	1.534	-	173.63	[20]
FeP/Fe$_2$O$_3$@NPCA	1.42	648 | 20	108	[21]
CNT@SAC-Co/NCP	1.45	864.8 | 5	172	[22]
CoFe@NC/NCHHSs	1.467	774.08 | 10	184	[23]
IrCo-N-C	1.46	-	138.8	[24]
Fe$_{20}$@N/HCSs	1.57	726.9 | 20	140.8	[25]
Ni@N-HCGHF	1.49	706 | 10	117.1	[26]

Table S5. Comparison of electrochemical performances of recently reported flexible Zn–air batteries with transition metal-based catalysts as cathodes.

Catalysts	Open-circuit voltage (V)	Peak power density (mW cm^{-2})	Cycling life	Reference
Fe-N@Ni-HCFS	1.43	64.5	10 h @2 mA cm^{-2}	This work
FeP/Fe_2O_3@NP CA	1.42	40.8	500 min @5 mA cm^{-2}	[21]
CS-NFO@PNC-700	1.32	51	40 h @5 mA cm^{-2}	[27]
Fe-Co_2P@Fe-N-C	1.24	21.9	24 cycles @2 mA cm^{-2}	[28]
$NiFe_2O_4$/CNTs	-	56	10 h @5 mA cm^{-2}	[29]
CoFe@NCNT/CFC	1.426	37.7	940 min @1 mA cm^{-2}	[30]
$Co(OH)_2$@NC	1.35	36.9	Over 400 min @5 mA cm^{-2}	[31]
CoS_x@Cu_2MoS_4-MoS_2/NSG	1.442	40	-	[32]
N-GQDs/$NiCo_2S_4$/CC	1.406	26.2	12 h	[33]
Co/Co–N–C	1.41	-	10 h @2 mA cm^{-2}	[34]

References

[1] L. Yu, J. F. Yang, B. Y. Guan, Y. Lu, X. W. Lou, *Angew. Chem. Int. Ed.* **2018**, *57*, 172.

[2] a) G. Kresse, J. Furthmüller, Comput. Mater. Sci. **1996**, *6*, 15. b) G. Kresse, D. Joubert, *Phys. Rev. B* **1999**, *59*, 1758.

[3] J. P. Perdew, K. Burke, M. Ernzerhof, Phys. Rev. Lett. **1996**, *77*, 3865.

[4] a) Mao, G. Kour, C. Yan, Z. Zhu, A. Du, *J. Phys. Chem. C* **2019**, *123*, 3703. b) S. Liu, Z. Wang, S. Zhou, F. Yu, M. Yu, C. Y. Chiang, W. Zhou, J. Zhao, J. Qiu, *Adv. Mater.* **2017**, *29*, 1700874; c) T. Duguet, E. Gaudry, T. Deniozou, J. Ledieu, M. C. de Weerd, T. Belmonte, J. M. Dubois, V. Fournée, *Phy. Rev. B* **2009**, *80*, 205412.

[5] S. Grimme, *J. Comput. Chem.* **2006**, *27*, 1787.

[6] Q. Lu, X. Zou, C. Wang, K. Liao, P. Tan, R. Ran, W. Zhou, M. Ni, Z. Shao, *Energy Storage Mater.* **2021**, *39*, 11.

[7] H. Lei, Z. Wang, F. Yang, X. Huang, J. Liu, Y. Liang, J. Xie, M. S. Javed, X. Lu, S. Tan, W. Mai, *Nano Energy* **2019**, *68*, 104293.

[8] G. T. Fu, Z. M. Cui, Y. F. Chen, L. Xu, Y. W. Tang, J. B. Goodenough, *Nano Energy* **2017**, *39*, 77.

[9] J. Chen, H. Li, C. Fan, Q. Meng, Y. Tang, X. Qiu, G. Fu, T. Ma, *Adv. Mater.* **2020**, *32*, 2003134.

[10] Z. Zhu, H. Yin, Y. Wang, C. H. Chuang, L. Xing, M. Dong, Y. R. Lu, G. Casillas-Garcia, Y. Zheng, S. Chen, Y. Dou, P. Liu, Q. Cheng, H. Zhao, *Adv. Mater.* **2020**, *32*, 2004670.

[11] X. Zhu, D. Zhang, C.-J. Chen, Q. Zhang, R.-S. Liu, Z. Xia, L. Dai, R. Amal, X. Lu, *Nano Energy* **2020**, *71*, 104597.

[12] Z. Li, Q. Wang, X. Bai, M. Wang, Z. Yang, Y. Du, G. E. Sterbinsky, D. Wu, Z. Yang, H. Tian, F. Pan, M. Gu, Y. Liu, Z. Feng, Y. Yang, *Energy Environ. Sci.* **2021**, *14*, 5035.

[13] X. Han, X. Ling, D. Yu, D. Xie, L. Li, S. Peng, C. Zhong, N. Zhao, Y. Deng, W. Hu, *Adv. Mater.* **2019**, *31*, 1905622.

[14] Y. Wang, Z. Li, P. Zhang, Y. Pan, Y. Zhang, Q. Cai, S. R. P. Silva, J. Liu, G. Zhang, X. Sun, Z. Yan, *Nano Energy* **2021**, *87*, 106147.

[15] Q. Shi, Q. Liu, Y. Ma, Z. Fang, Z. Liang, G. Shao, B. Tang, W. Yang, L. Qin, X. Fang, *Adv. Energy Mater*. **2020**, *10*, 1903854.

[16] D. Ren, J. Ying, M. Xiao, Y. P. Deng, J. Ou, J. Zhu, G. Liu, Y. Pei, S. Li, A. M. Jauhar, H. Jin, S. Wang, D. Su, A. Yu, Z. Chen, *Adv. Funct. Mater*. **2020**, *30*, 1908167.

[17] Y. Niu, X. Teng, S. Gong, M. Xu, S. G. Sun, Z. Chen, *Nano-Micro Lett*. **2021**, *13*, 126.

[18] M. Wu, G. Zhang, J. Qiao, N. Chen, W. Chen, S. Sun, *Nano Energy* **2019**, *61*, 86.

[19] T. Cui, Y. P. Wang, T. Ye, J. Wu, Z. Chen, J. Li, Y. Lei, D. Wang, Y. Li, *Angew. Chem. Int. Ed*. **2022**, *61*, e202115219.

[20] Y. R. Hao, H. Xue, L. Lv, J. Sun, N. Guo, T. Song, H. Dong, J. Zhang, Q. Wang, *Appl. Catal. B*: *Environ*. **2021**, *295*, 120314.

[21] K. Wu, L. Zhang, Y. Yuan, L. Zhong, Z. Chen, X. Chi, H. Lu, Z. Chen, R. Zou, T. Li, C. Jiang, Y. Chen, X. Peng, J. Lu, *Adv. Mater*. **2020**, *32*, 2002292.

[22] J. C. Li, Y. Meng, L. Zhang, G. Li, Z. Shi, P. X. Hou, C. Liu, H. M. Cheng, M. Shao, *Adv. Funct. Mater*. **2021**, *31*, 2103360.

[23] S. Wang, H. Wang, C. Huang, P. Ye, X. Luo, J. Ning, Y. Zhong, Y. Hu, *Appl. Catal. B*: *Environ*. **2021**, *298*, 120512.

[24] M. Xiao, J. Zhu, S. Li, G. Li, W. Liu, Y.-P. Deng, Z. Bai, L. Ma, M. Feng, T. Wu, D. Su, J. Lu, A. Yu, Z. Chen, *ACS Catal*. **2021**, *11*, 8837.

[25] B. Wang, Y. Ye, L. Xu, Y. Quan, W. Wei, W. Zhu, H. Li, J. Xia, *Adv. Funct. Mater*. **2020**, *30*, 2005834.

[26] L. Yan, Y. Xu, P. Chen, S. Zhang, H. Jiang, L. Yang, Y. Wang, L. Zhang, J. Shen, X. Zhao, L. Wang, *Adv. Mater*. **2020**, *32*, 2003313.

[27] S. Ramakrishnan, D. B. Velusamy, S. Sengodan, G. Nagaraju, D. H. Kim, A. R. Kim, D. J. Yoo, *Appl. Catal. B*: *Environ*. **2021**, *300*, 120752.

[28] X. W. Lv, W. S. Xu, W. W. Tian, H. Y. Wang, Z. Y. Yuan, *Small* **2021**, *17*, 2101856.

[29] N. Xu, Y. Zhang, T. Zhang, Y. Liu, J. Qiao, *Nano Energy* **2019**, *57*, 176.

[30] L. Liu, X. Zhang, F. Yan, B. Geng, C. Zhu, Y. J. Chen, *J. Mater. Chem. A* **2020**, *8*, 18162.

[31] Y. Wang, A. Li, C. Cheng, *Small* **2021**, *17*, 2101720.

[32] D. C. Nguyen, D. T. Tran, T. L. L. Doan, D. H. Kim, N. H. Kim, J. H. Lee, *Adv. Energy Mater*. **2020**, *10*, 1903289.

[33] W. Liu, B. Ren, W. Zhang, M. Zhang, G. Li, M. Xiao, J. Zhu, A. Yu, L. Ricardez-Sandoval, Z. Chen, *Small* **2019**, *19*, 1903610.

[34] P. Yu, L. Wang, F. Sun, Y. Xie, X. Liu, J. Ma, X. Wang, C. Tian, J. Li, H. Fu, *Adv. Mater*. **2019**, *31*, 190166.